A novel approach for seismoelectric measurements using multielectrode arrangements - II: laboratory measurements

M.S. Devi, S. Garambois, Daniel Brito, M. Dietrich, V. Poydenot, Clarisse Bordes

Geophysical Journal International

Geophys. J. Int. (2018) **214,** 1783–1799
Advance Access publication 2018 June 21
GJI Marine geosciences and applied geophysics

doi: 10.1093/gji/ggy251

A novel approach for seismoelectric measurements using multielectrode arrangements: II—Laboratory measurements

M. S. Devi,[1] S. Garambois,[1] D. Brito,[2] M. Dietrich,[1] V. Poydenot[2] and C. Bordes[2]

[1] *Univ. Grenoble Alpes, Univ. Savoie Mont Blanc, CNRS, IRD, IFSTTAR, ISTerre, UMR* 5275, 38000 *Grenoble, France. E-mail: Stephane.Garambois@univ-grenoble-alpes.fr*

[2] *Univ. Pau & Pays Adour, /TOTAL/CNRS, Laboratoire des Fluides Complexes et leurs Rservoirs–IPRA, UMR* 5150, *Pau, 64000, France*

Accepted 2018 June 20. Received 2018 March 27; in original form 2018 June 18

SUMMARY

Transient electrokinetic effects may generate conversions between seismic and electromagnetic energy in fluid-filled poroelastic media. Two resulting seismoelectric signals have been predicted and identified: on the one hand electric fields accompanying seismic waves and on the other hand electromagnetic disturbances generated when seismic waves are crossing interfaces. The coseismic electrical field is in general the dominant effect, but it only provides local information around the electrical receivers. On the contrary, the seismoelectric interface response could be exploited in a new high-resolution imaging technique, as it is particularly sensitive to fluid contrasts. However, the detection of such events is a challenging task, mainly because it is usually masked by the higher amplitude coseismic electric field and by the presence of strong electrical noise. In order to increase the signal-to-noise ratio of the interface response, we experimentally study the sensitivity of seismoelectric signals to various electrode arrangements used for their recording. For that, we use a filter theory approach to investigate the response of electrode arrays to measure seismoelectric signals. Then, we confront this approach with seismoelectric data acquired in homogeneous silica glass-beads in laboratory experiments. The measured laboratory coseismic signals were also successfully compared with numerical simulations, which in turn have been used to predict the sensitivity of the interface electromagnetic signals to the data acquisition configuration. This study demonstrates the possibilities offered by multielectrode arrays to enhance the electromagnetic interface response.

Key words: Numerical modelling; Hydrogeophysics; Electromagnetic theory; Wave propagation; Eelectrical Properties; Permeability and porosity.

1 INTRODUCTION

The propagation of elastic waves in a wet porous medium induces relative movements between the fluid and the grain matrix. This produces an electric field localized within seismic waves, namely, a coseismic electric field, due to an electrokinetic phenomenon (Ivanov 1939; Broding *et al.* 1963; Long & Rivers 1975). This electrokinetic phenomenon is itself explained by the presence of an electrical double layer at the grain–fluid interface. In addition, when seismic wave fronts cross an interface between two media exhibiting contrasts of mechanical and/or electrical properties, an electromagnetic (EM) disturbance is radiated from that interface because of the time-varying imbalance of the streaming currents on both sides (see for a review Jouniaux & Zyserman 2016). The interface response was observed in field experiments performed in the near-surface by Martner & Sparks (1959), who recorded EM precursors to seismic arrival, indicating a wave with very high velocity generated at the base of a weathered layer.

Based on a series of large-scale field experiments, Thompson & Gist (1993) suggested that the seismoelectric coupling mechanism has the potential to directly detect fluids at depth with a high resolution. This observation, as well as the theoretical developments of Pride (1994), has motivated seismoelectric investigations in the shallow subsurface (Butler *et al.* 1996; Mikhailov *et al.* 1997; Beamish 1999; Garambois & Dietrich 2001; Dupuis *et al.* 2007; Haines *et al.* 2007a; Strahser *et al.* 2007). Despite advances in signal processing, such as the fast discrete curvelet transform (Warden *et al.* 2012), this promising exploration method remains challenging to use because of the low signal-to-noise (S/N) ratio of the records and the presence of high-amplitude coseismic signals, which mask EM arrivals generated at interfaces.

The seismoelectric signals are generally recorded by using pairs of electrodes (electric dipoles) connected to a digitizer. This setup is

used to measure the electric field as a voltage difference. As already mentioned above, seismoelectric signals are usually dominated by noise consisting of 50 or 60 Hz powerline disturbances and their harmonics (see e.g. Butler *et al.* 1996; Mikhailov *et al.* 1997; Russell *et al.* 1997; Garambois & Dietrich 2001; Sorokina & Bulychov 2001; Rosid & Kepic 2004; Dupuis *et al.* 2007; Haines *et al.* 2007b). Another source of electrical noise are atmospheric transients (sferics) due to distant lightning strikes and electrical storms (Macnae *et al.* 1984; Butler *et al.* 1996; Kepic & Butler 2002; Norvill & Kepic 2004). A significant part of these interferences can be mitigated via post-processing, in particular by using the adaptive powerline noise subtraction technique of Butler & Russell (2003). Another option to reduce man-made disturbances, which can be applied directly in the field, is to use electrode arrays instead of dipoles, as originally tested by Thompson (1936) for seismoelectric signals. This approach will be developed below.

The second issue for seismoelectric exploration is that the seismoelectric data mainly consist of coseismic electrical signals, and particularly the electrical signature of dispersive Rayleigh surface waves when the data are recorded along the ground surface (e.g. Long & Rivers 1975; Garambois & Dietrich 2001). In industrial seismic reflection surveys, geophone arrays have long been used to favour near-vertical seismic reflections and attenuate at the same time unwanted surface-wave arrivals (see e.g. Hales & Edwards 1955; Knapp & Steeples 1986a,b). As with geophone arrays, arrangements of electrodes could be designed to mitigate coseismic contributions while preserving the targeted EM interface responses.

So far, seismoelectric fields have been systematically investigated from electrical potential differences measured using electrical dipoles. Their sensitivity to dipole characteristics (dipole length, burial depth) and electrode ground coupling properties have been studied in the field (see e.g. Mikhailov *et al.* 1997; Beamish 1999; Haines *et al.* 2007a; Dupuis *et al.* 2007), without leading to significant improvements for interface response detection. Enhancing the weak signals characterizing seismoelectric measurements has been attempted by connecting the electrical dipoles to a pre-amplifier (Kepic & Butler 2002), by choosing a powerful seismic source (Bulychov 2005; Dean & Valuri 2012), by stacking individual seismoelectric shots (see e.g. Beamish 1999; Mikhailov *et al.* 1997; Garambois & Dietrich 2001), by using supergathers (Dupuis *et al.* 2007) or by measuring seismoelectric data nearby interfaces, in boreholes (Dupuis *et al.* 2009). It seems that recording of seismoelectric signals with electric dipoles arrangement has never been questioned as a measuring technique. Still, the interface response, which shows up as quasi-plane waves parallel to the ground surface, appears with very weak amplitudes, notably because these amplitudes are significantly attenuated when electrical dipoles are used for its recording, as suggested by Dietrich *et al.* (2018) in a companion paper. This may partly explain why interface response was only clearly recorded in a limited number of field studies (see e.g. Garambois & Dietrich 2001; Bulychov 2003; Dupuis *et al.* 2007; Haines *et al.* 2007b), and at interfaces between water and rock samples in laboratory experiments (Zhu *et al.* 2008; Schakel *et al.* 2011). The purpose of this paper is to present experimental investigations at the laboratory scale of the novel seismoelectric recording approach suggested by Dietrich *et al.* (2018), which takes benefit of electrode arrays.

During the last two decades, seismoelectric laboratory experiments have been performed for various studies, for example, to study the sensitivity to conductivity in micro glass-beads and medium-grain sands (Chen & Mu 2005; Block & Harris 2006; Holzhauer *et al.* 2017). Besides seismoelectric experiments, seismomagnetic measurements were also performed by Zhu & Toksoz (2005) and by Bordes *et al.* (2008). More recently, the influence of water saturation on coseismic signals was examined experimentally and theoretically by Bordes *et al.* (2015), whereas the sensitivity of seismoelectric amplitudes to the length of dipoles was established by Holzhauer *et al.* (2017). In all these studies, the seismoelectric signals were measured using electrical dipole.

In this paper, we consider alternative electrode configurations and investigate the influence of the electrode arrangement on seismoelectric responses, by confronting the filter theory and numerical developments proposed by Dietrich *et al.* (2018) to real laboratory data. We first briefly recall the basics of this filter properties generated by specific electrode arrangements, which are thoroughly described in a companion paper (Dietrich *et al.* 2018). We then present laboratory coseismic signals obtained using various electrode arrangements, by varying the array length L, the number of the electrodes and the apparent seismic velocity. These results are compared with theoretical predictions and full waveform numerical simulations performed using the seismoelectric modelling code adapted by Dietrich *et al.* (2018) to compute electrical potential. This successful confrontation allows numerical studies highlighting the benefits of using different electrode arrangements to amplify an interface response compares to coseismic arrivals.

2 SIGNATURE OF ELECTRODE ARRANGEMENT ON SEISMOELECTRIC SIGNALS: ANALYTICAL APPROACH

The approach used is inspired from the concept of arrays of geophones in reflection seismology, which was developed to favour near-vertical seismic reflections by attenuating unwanted surface waves (Hales & Edwards 1955). In seismic exploration, the procedure essentially consists in deploying, for each trace, a few geophones connected in series, usually in line with direction of the profile, so that the signals of interest (reflected waves) are in-phase and stacked constructively along the geophone array, while the dispersive surface waves are mostly out-of-phase and thus partly removed (Knapp & Steeples 1986a). The filtering achieved by a linear array of geophones depends on the properties of the receiver array (number of receivers and array length), and on the characteristics of the incoming (plane) wave (angle of emergence and frequency).

A somewhat similar multielectrode approach has been proposed by Thompson (1936) for electrical measurements, with linear arrays of three to five electrodes with constant spacing. At the time, the so-called ‘seismic electric effect’ was referring to disturbances generated by seismic waves’ propagation when measuring electrical resistivity. These multielectrode configurations were tested to reduce the background electrical noise to enhance the seismic electric effect. Thompson (1936) introduced configurations with an odd number of electrodes in which every other electrode is assigned the same polarity. Positive electrodes are connected together, and negative electrodes as well. The observed signal is measured between these two groups of electrodes, as illustrated in fig. 3 of Dietrich *et al.* (2018).

To quantitatively describe the measurements of a seismoelectric wavefield, Dietrich *et al.* (2018) consider the electrical signature of a seismic plane wave propagating with a single angular frequency ω, which reaches the ground surface from below with an angle θ relative to the ground surface (fig. 1 of Dietrich *et al.* 2018). The incident angle θ, the array length L between the two outer electrodes and the wave velocity V determine a horizontal delay time τ_x, which

corresponds to the time needed by the plane wave to propagate from electrode e_1 to electrode e_2:

$$\tau_x = \frac{L}{V_{ax}} = \frac{L \sin\theta}{V}, \quad (1)$$

where V_{ax} is the apparent velocity of the wave front along the ground surface and $1/V_{ax}$ is the horizontal slowness of the wave front.

In general, seismoelectric fields are measured from the voltage difference between two electrodes $\Delta v(t)$:

$$E(t) \simeq \frac{\Delta v(t)}{d} = \frac{v_1(t) - v_2(t)}{d} = \frac{v_1(t)}{d} * [\,\delta(t) - \delta(t - \tau_x)\,], \quad (2)$$

$v_i(t)$ being the potential at electrode i, $\delta(t)$ the Dirac delta function and symbol $*$ denoting the convolution operator.

From eq. (2), it becomes clear that this dipole configuration strongly attenuates the EM interface responses which manifest themselves by quasi-plane waves arriving more or less parallel to the ground surface ($\tau_x \approx 0$) and with virtually the same amplitude over the small distance L involved (Garambois & Dietrich 2001).

The electric signals $s_{iel}(t)$ can be directly measured by connecting together electrodes e_1 to e_5 as described in fig. 3 of Dietrich *et al.* (2018), *iel* being the number of electrodes included in one single measurement. This results in

$$s_{2el}(t) = v_1(t) - v_5(t) \quad (3)$$

$$s_{3el}(t) = v_1(t) - v_3(t) + v_5(t) \quad (4)$$

$$s_{5el}(t) = v_1(t) - v_2(t) + v_3(t) - v_4(t) + v_5(t). \quad (5)$$

Considering the various electrode configurations presented in Dietrich *et al.* (2018) we can write $s_{3el}(t) = v_1(t) - v_2(t) + v_3(t)$ for an array of three electrodes and $s_{5el}(t) = v_1(t) - v_2(t) + v_3(t) - v_4(t) + v_5(t)$ for an array of five electrodes. Dietrich *et al.* (2018) shows that the modulus of the complex gain of the filters corresponding to two, three and five electrodes are respectively

$$|G_{2el}(\omega)| = 2|\sin(\omega\tau_x/2)| \quad (6)$$

$$|G_{3el}(\omega)| = |2\cos(\omega\tau_x/2) - 1| \quad (7)$$

$$|G_{5el}(\omega)| = |2\cos(\omega\tau_x/2) - 2\cos(\omega\tau_x/4) + 1|. \quad (8)$$

One should especially notice that the dipole configuration is associated with a sine function, whereas the three- and five-electrode configurations are described by cosine functions. Small values of the horizontal delay time τ_x correspond to small values of the filter response G_{2el}, thereby explaining the considerable attenuation of plane-waves arriving more or less parallel to the ground surface. With the three- and five-electrode configurations, the filter response is equal to 1 when $\tau_x = 0$. As illustrated analytically and numerically by Dietrich *et al.* (2018), the properties of these filters modify the seismoelectric spectral responses, depending on the number of electrodes, the array length L and the apparent velocity of incoming waves (eq. 1). In this paper, we propose to experimentally confirm this crucial result by recording and analysing coseismic electrical data measured in a homogeneous material in laboratory conditions.

3 SEISMIC AND SEISMOELECTRIC DATA ACQUISITION

3.1 Experimental setup

Seismic and seismoelectric experiments were carried out at the laboratory scale using a piezoelectric transducer source (from 0.1 to 1 MHz with an optimal frequency around 250 kHz), which generates mainly *P*-waves propagating in a homogeneous water-saturated porous medium. An output from a function generator has been set as one cycle of sine wave with a predetermined main frequency. This device was plugged into a high voltage amplifier featuring a $\pm$ 150 V maximum supply voltage which was eventually connected to the longitudinal piezoelectric transducer (Fig. 1).

Seismoelectric responses to various electrode arrangements were studied using an array of mini-electrodes consisting in 30 stainless-steel rods with diameter of 0.2 mm and length of 50 mm. These adjacent electrodes were spaced every 2.5 mm. The first e_1 and last e_{30} electrodes were placed respectively at 50 and 123 mm from the source. This array allows us to measure the electric signals acquired with two-, three- and five-electrode configurations considering various array lengths L, apparent velocities V_{ax} and angular frequencies ω. It must be noted that the array lengths considered in our laboratory conditions (from half the seismic wavelength λ to 4λ) are greater than those classically used in the field (typically a tenth of λ). However, this does not alter the confrontation between the filter theory developed by Dietrich *et al.* (2018) and real data.

A laser *Doppler* vibrometer was used to measure the normal seismic displacements at the sample surface (e.g. Lebedev *et al.* 2011). The system consists of a OFV-505 single point laser head and a DD-300 auxiliary (displacement) decoder. The vertical particle displacement u_z is obtained from the frequency shift of a scattered helium-neon laser on a reflective tape which has been placed on the surface of the porous material. A scaling factor for the displacement decoder is given as 50 nm V^{-1}.

Unconsolidated synthetic glass beads, mainly composed of quartz with grain sizes of 125–160 μm were used as a porous medium. They were poured into a plastic box of 220 $\times$ 160 $\times$ 70 mm, and were eventually gently shaken. The glass-beads were washed several times (Glover & Dery 2010) and then saturated by demineralized water, leading to an initial fluid conductivity of $\sim$25 μS cm^{-1} (corresponding approximately to a salinity of 4 $\times 10^{-4}$ mol l^{-1}), measured at equilibrium state. This value may increase over time when water is in contact with the glass beads.

Seismic and seismoelectric signals were recorded simultaneously after stacking signals 2000 times using a four channel *Keysight* DSO-S 054A digital storage oscilloscope with a 10 MHz sampling frequency on a duration of 2 ms, which includes a 0.4 ms window before triggering. We could not measure seismic displacements in the horizontal plane (see Fig. 1), since the displacement can only be measured along the direction of the laser beam of the interferometer. As observed by Garambois & Dietrich (2001, 2002), the horizontal components of electric field E_h should be quantitatively compared in theory with the horizontal component of the grain acceleration $\ddot{u}_h$. Nevertheless, comparing the arrival time and frequency content of E_h and $\ddot{u}_z$ can be reasonably performed as qualitatively displayed on field data by Garambois & Dietrich (2001) in their fig. 4.

3.2 On the need of a reference electrode

In seismoelectric observations, the choice of the electrode spacing results from a compromise between the need of local electric field measurements and S/N ratio issues. When electrical noise is small enough and spatially constant, the use of a reference electrode positioned at infinity will increase the number of effective traces (Holzhauer *et al.* 2017). In this case, the local electric field is reconstituted from the subtraction of two voltage difference measurements performed between a given electrode and the reference

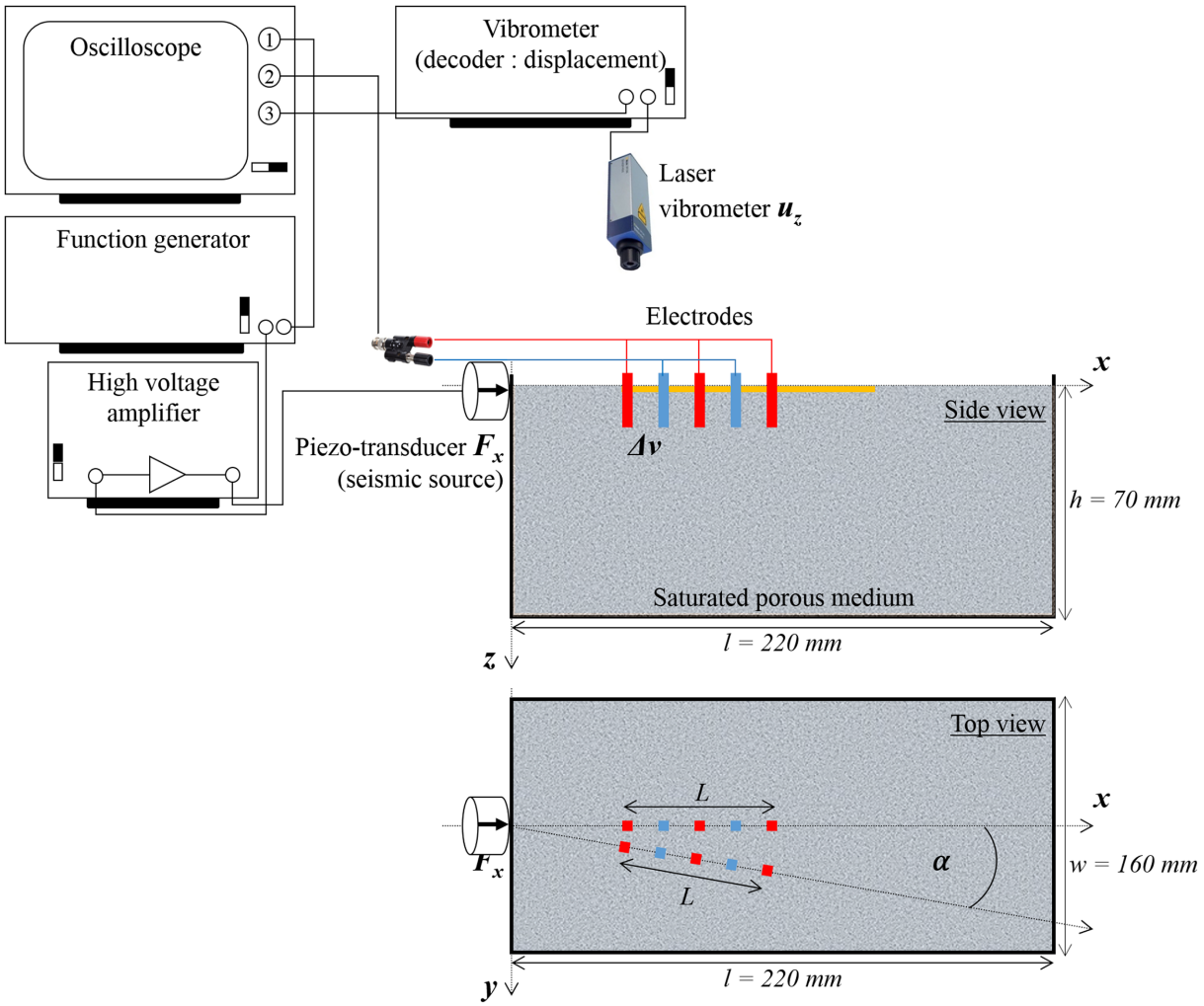

Figure 1. Side and top views of the laboratory experimental setup and the acquisition chain. A piezoelectric transducer generates seismic waves, whose surface displacements are recorded using a laser vibrometer while seismoelectric signals are recorded using electrode arrays. By rotating the receiver line by an angle α, different apparent seismic velocities are generated.

one. However, in field experiments, the use of a reference electrode is often not possible, because stable low-noise conditions are not met, resulting in weak S/N ratio. In our laboratory conditions, we could measure the electric signals $D_n(t) = v_n(t) - v_{30}(t)$ between the reference electrode e_{30} (the farthest from the source, with an offset of 123 mm) and the electrode numbered e_1 to e_5, that is, with dipole lengths ranging from 73 to 63 mm.

Consequently, the electric signals with respect to a reference electrode, denoted here $\tilde{s}_{iel}(t)$ for each electrode configuration can be deduced from the $D_n(t)$ measurements:

$$\tilde{s}_{2el}(t) = D_1(t) - D_5(t) \tag{9}$$

$$\tilde{s}_{3el}(t) = D_1(t) - D_3(t) + D_5(t) \tag{10}$$

$$\tilde{s}_{5el}(t) = D_1(t) - D_2(t) + D_3(t) - D_4(t) + D_5(t). \tag{11}$$

We display in Fig. 2 the seismoelectric signals generated by a 200 kHz longitudinal excitation and recorded using the two-, three- and five-electrode arrays with an array length L of 10 mm. A comparison of the two electric signals $\tilde{s}_{iel}(t)$ and $s_{iel}(t)$ is highlighted. Figs 2(a) and (b) show the spatial evolution of the potential difference $D_n(t)$ for n varying from 1 to 5. It highlights three different types of electrical signals : (i) a large dominating instantaneous signal (labelled 1), which is in-phase on all the measurements $D_1(t)$ to $D_5(t)$, (ii) coseismic signals propagating with a given apparent velocity and (iii) residual electrical noise. It is noticeable that the coseismic signals are due to the direct P-wave when it reaches electrodes e_n (labelled 2) and when it reaches the reference electrode (labelled 4) as well as reflected waves at the edges (labelled 3). The large electrical noise originating at $t = 0$ is due to the electrical triggering of the piezoelectric transducer and appears synchronous on all voltage measurements displayed in Fig. 2(b). This disturbance is emitted in the air and can be captured by any part of the recording chain. Figs 2(c) and (d) highlight for the three electrode configurations a comparison of the recorded signals $\tilde{s}_{iel}(t)$ and $s_{iel}(t)$ respectively acquired between electrodes e_1 and e_5 with (red line) and without (blue line) the use of the reference electrode e_{30}. At first order, we observe that both measurement methods give substantially the same results. The use of a reference electrode with an odd number of electrodes introduces an additional propagating coseismic electrical signal $v_{30}(t)$, when the seismic waves impinges the reference electrode, which is not suitable when local seismoelectric fields have to be recorded. It also shows that for the two-electrode configuration, the double difference measurement method (with a

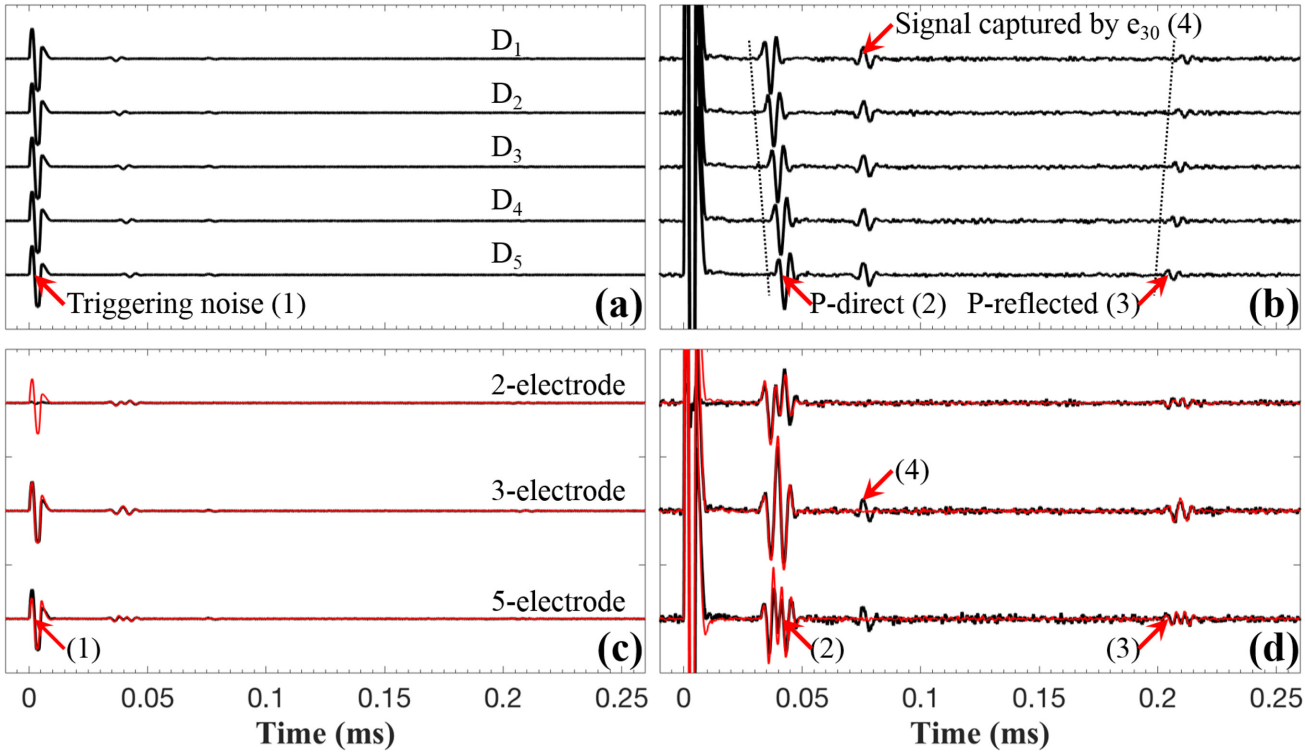

Figure 2. (a) Raw and (b) amplified voltage differences $D_n(t)$ for five inner electrode locations (50–60 mm). Comparison of raw (c) and amplified (d) local electrical potential differences $\tilde{s}_{iel}(t)$ measured at e_1 as inner electrode and using a reference electrodes e_{30} (red lines) and $s_{iel}(t)$ obtained directly from different connections (blue lines) for the 2- (top), 3- (middle) and five-electrode (bottom) arrangements with an array length L of 10 mm.

Table 1. Signal-to-noise ratios for different electrode configurations and array lengths L.

Configuration	Array length L (mm)	S/N reference	S/N no-reference
Two-electrode	2.5	8.0	80.0
	5.0	9.5	42.8
	7.5	6.6	14.7
	10.0	8.4	12.3
Three-electrode	5.0	7.9	16.7
	10.0	9.5	19.4
Five-electrode	10.0	4.7	15.5

reference electrode) efficiently removes the synchronous triggering noise at $t = 0$.

Quantitative S/N ratio have been estimated by peak-to-peak amplitude measurements considering signal (2) and noise recorded before the triggering (Table 1). For all tested configurations and array lengths, the use of a reference electrode increases the level of ambient electrical noise, which affects the S/N ratios.

These experiments also show that the coseismic waveforms strongly differ according to the electrode configuration, as well as their S/N ratio. These properties will be studied hereafter.

3.3 Quantitative illustration of electrode configuration influence on seismoelectric waveforms

Seismic and seismoelectric raw data acquired using a 200 kHz source for various offsets are displayed in Fig. 3. Seismic traces displayed in Figs 3(a) and (b) were acquired close to the inner electrode for each configuration. Seismoelectric data shown in Figs 3(c) and (d) are $s_{2el}(t)$ and $s_{3el}(t)$ measured for different offsets with an array length L=5 mm. The line of receivers was placed with an angle $\alpha = 22.5^o$ with respect to the seismic wave front (Fig. 1).

The triggering noise (labelled *(1)* in Fig. 3c) dominates seismoelectric data, but other events are consistent in all recordings : *P-direct (2)* and *P-reflected* waves (from the bottom of the box denoted as *P-reflected 3*) which propagate with an apparent velocity of $\sim$2010 m s^{-1} can be identified. We also noticed *P-reflected 4* waves coming from the end side of the box. In the seismic data, a late low-velocity weak arrival was identified as the sound wave (labelled *5*, apparent velocity of 380 m s^{-1}). The seismoelectric waveforms differ depending on the electrode configuration used for their recording. These waveforms are further analysed regarding the filter properties associated to each electrode configuration (eqs 6–8) after basic signal processing have been applied to raw data in order to isolate the seismoelectric signals. For that, a simple time windowing was applied to the data, as illustrated in Fig. 4 on a single trace located at an offset of 74 mm. This figure shows data in time and frequency domains for both seismic and seismoelectric data (two- and three- electrode configurations). The seismoelectric waveforms and spectra differ according to the electrode arrangement, while no seismic acceleration change was noticed. The three-electrode seismoelectric spectrum (c) exhibits a higher frequency content than the seismic acceleration (a) and the two-electrode (b) spectra.

When using a dipole, the differences between acceleration and the derived seismoelectric fields may result from two different frequency-dependent effects : the seismoelectric transfer function $TF_{EK}(\omega)$ (Garambois & Dietrich 2001) and the electrode arrangement filter function $G_{2el}(\omega)$. For other arrays, the pseudo-electric field was obtained from the $s_{iel}(t)$ measurements after a division by the array length. Consequently, the coseismic recorded

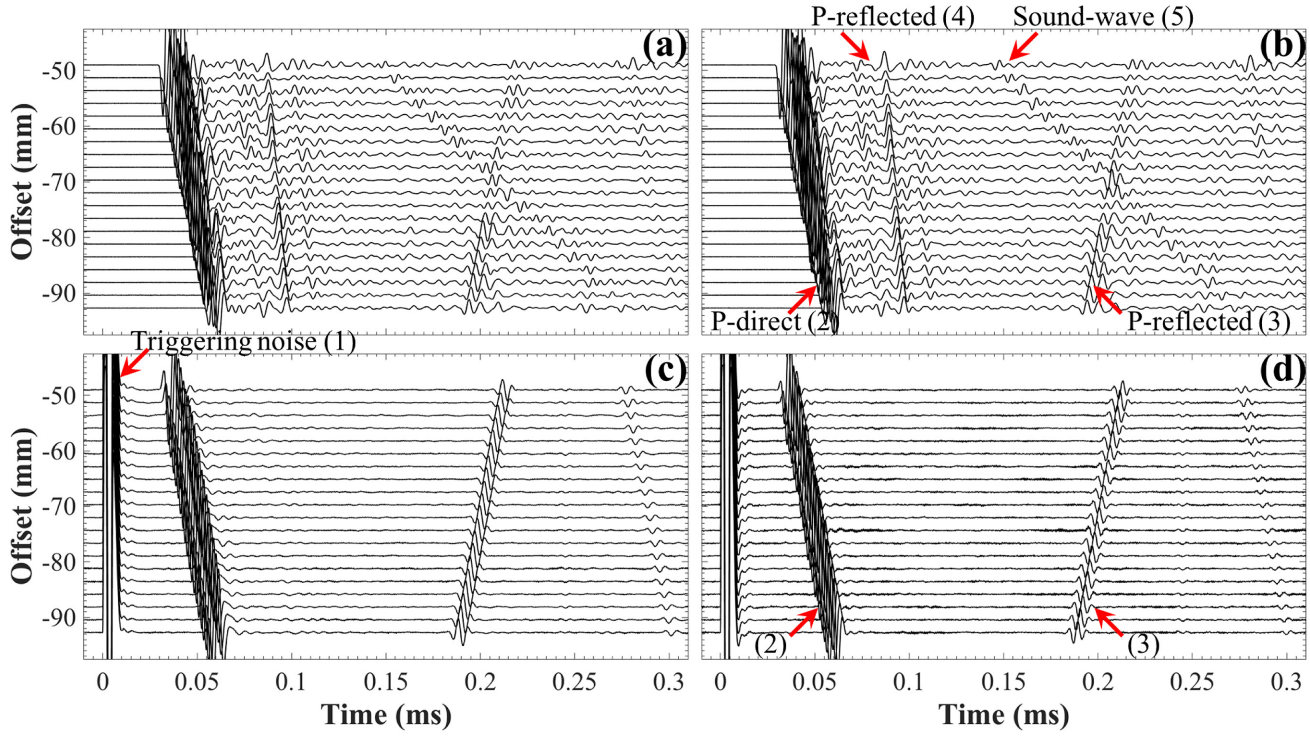

Figure 3. Seismic (a) and seismoelectric data (c) recorded with an array length L of 5 mm in the two-electrode configuration and generated with a source frequency of 200 kHz. (b) Seismic and (d) seismoelectric data recorded for the three-electrode configuration.

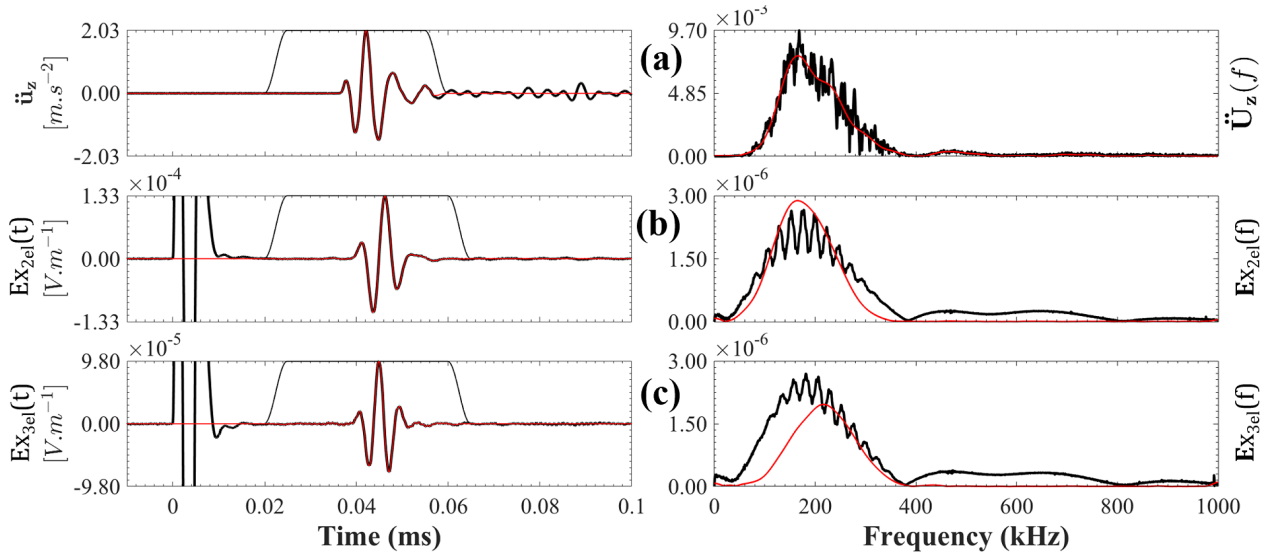

Figure 4. Vertical seismic accelerations (a) and seismoelectric data (b and c) displayed in the time domain before (black lines) and after tapering (red lines) with a trapezoidal time window and the corresponding spectra (right). The electric fields were deduced from voltage differences $\Delta v_{2-el}(t)$ (b) and $\Delta v_{3-el}(t)$ (c) after a division by the array length.

(pseudo-)electric field $\mathbf{E_{iel}}(\omega)$, which is generated by the propagation of a *P*-wave, can be written in the Fourier domain as

$$\mathbf{E_{iel}}(\omega) = G_{iel}(\omega) \cdot TF_{EK}(\omega) \cdot \ddot{\mathbf{u}}(\omega) \tag{12}$$

where $\ddot{\mathbf{u}}(\omega)$ is the particle acceleration spectrum and $G_{iel}(\omega)$ is the complex gain of the array filter considering i electrodes (eqs 6–8).

A quantitative analysis of eq. (12) is provided in Fig. 5 for the trace located at an offset of 74 mm. For that, we i) used the vertical acceleration spectra measured in the vicinity of the first electrode located at offset 74 mm (a), ii) computed the theoretical seismoelectric transfer function $|TF_{EK}(\omega)|$ (b) for the studied material using properties described in Table 2 after adjusting the fluid conductivity and iii) computed the theoretical frequency response of two- and three-electrode arrays with a velocity of 2010 m s^{-1} and an array length L of 5 mm. This figure illustrates the importance of the array filter response (c) on the final seismoelectric spectra variations. Indeed, the presence of lobes and zeros, whose locations and amplitudes vary according to the electrode arrangement, primarily

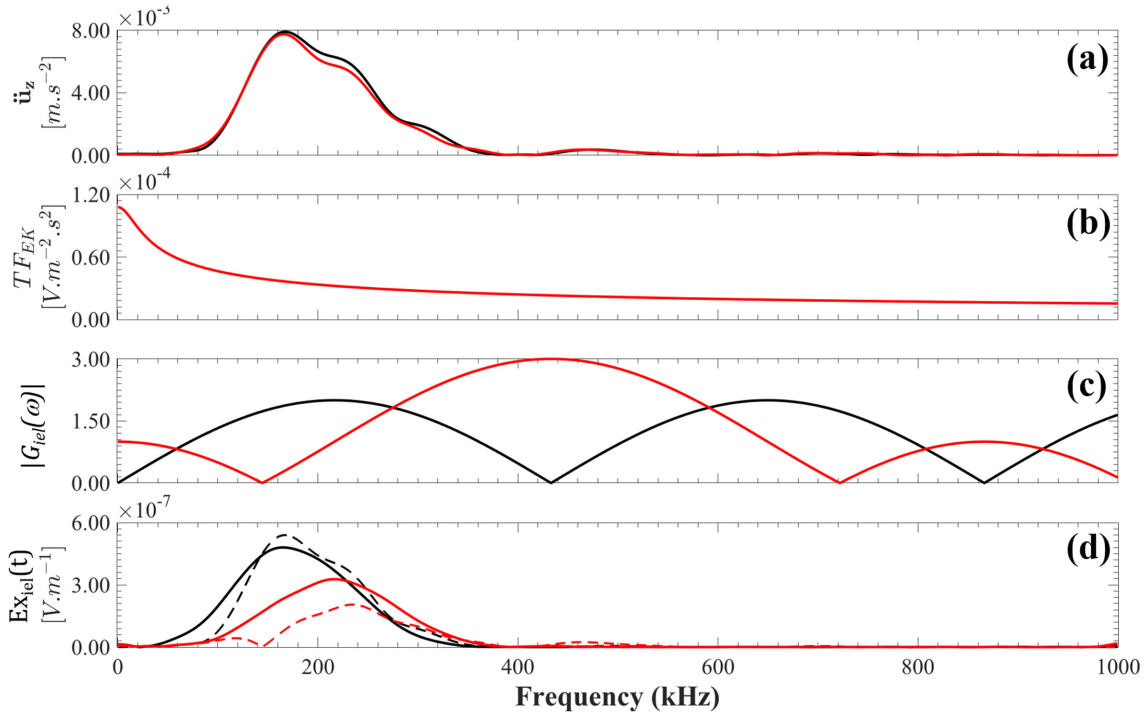

Figure 5. Results of the experiments considering two-electrode (red line) and three-electrode (black line) arrays. (a) Vertical seismic acceleration spectra; (b) predicted seismoelectric transfer function $|TF_{EK}(\omega)|$ using a salinity of 0.0125 mol l^{-1}; (c) spectral response of the array arrangement considering an array length L of 5 mm and a velocity of 2010 m s^{-1}. (d) Electric field comparison between observations (plain lines) and predictions (dashed lines) for the two-electrode (black) and three-electrode (red) arrays. The absolute accelerations and electric field amplitude were obtained after dividing the recorded data by the source stack number.

Table 2. Properties of the materials used for the numerical calculations

Input parameter	Material 1	Material 2
Porosity ϕ ()	40%	20%
Permeability k_0 (m^2)	10^{-12}	10^{-13}
Tortuosity $\mathcal{T}$ ()	1.75	1.75
Solid bulk modulus k_s (GPa)	36	36
Frame bulk modulus k_{fr} (GPa)	0.4	5.0
Shear modulus G_{fr} (GPa)	0.5	7.0
Solid density ρ_s (kg m^{-3})	2400	2700
Relative solid permittivity κ_s ()	4	4
Fluid bulk modulus k_f (GPa)	2.2	2.2
Fluid density ρ_f (kg m^{-3})	1000	1000
Fluid viscosity η (Pa s)	10^{-3}	10^{-3}
Fluid salinity C (mol l^{-1})	0.04	0.04
Relative fluid permittivity κ_f ()	80	80
Temperature T (K)	298	298

affects the final seismoelectric frequency response. On the contrary, the seismoelectric transfer function (b), which varies continuously over the whole frequency band, weakly affects the seismoelectric final response.

The recorded spectra for both electrode arrays (plain lines) are compared with the predicted spectra (dashed lines) defined by eq. (12) after the seismoelectric transfer function $|TF_{EK}(\omega)|$ was optimized using the water salinity (value of 0.0125 mol l^{-1}). This comparison shows that the measured seismoelectric spectra and their variations are well described by eq. (12). This comparison shows that the electrode array generates dominant filters, which primarily affect the seismoelectric recorded spectra. Indeed, in this case, the response is almost maximum at 175 kHz with the two-electrode array, while it is strongly attenuated with the three-electrode array at this frequency, as is the array filter.

In terms of amplitude, we computed the coseismic recorded electric field from the $s_{iel}(t)$ measurements, although we do not satisfy the ideal conditions observed by Holzhauer *et al.* (2017) who claim the distance between electrodes L should be lower than $\lambda/5$ (in our experiment, $d \simeq \lambda/2$). Consequently, the derived electric field could be underestimated. Here, the transfer function was optimized using a rather high water conductivity value in order to mimic the observed amplitudes, a value which seems one order of magnitude too high when compared to in-situ water conductivity measurements. This small discrepancy might be explained i) by the use of the vertical component of the acceleration for the comparison, where only longitudinal component should have been used; ii) by an increase of water conductivity when in contact with the grains and iii) by the underestimation of the electric field due to the large array length L. Consequently, in the following, only normalized comparisons between theory and observations will be performed, in order to focus on the filtering effects generated by the recording array properties.

4 PROPERTIES OF THE ELECTRODE CONFIGURATION FILTER

In this section, we experimentally study the sensitivity of the seismoelectric signals to the main parameters describing the electrode arrangements, that is, number of electrodes, array length and apparent velocity of the incoming seismic wave. These observations are systematically confronted to the expected variations predicted by the electrode-arrangement filters derived in the frequency domain (eqs 6–8).

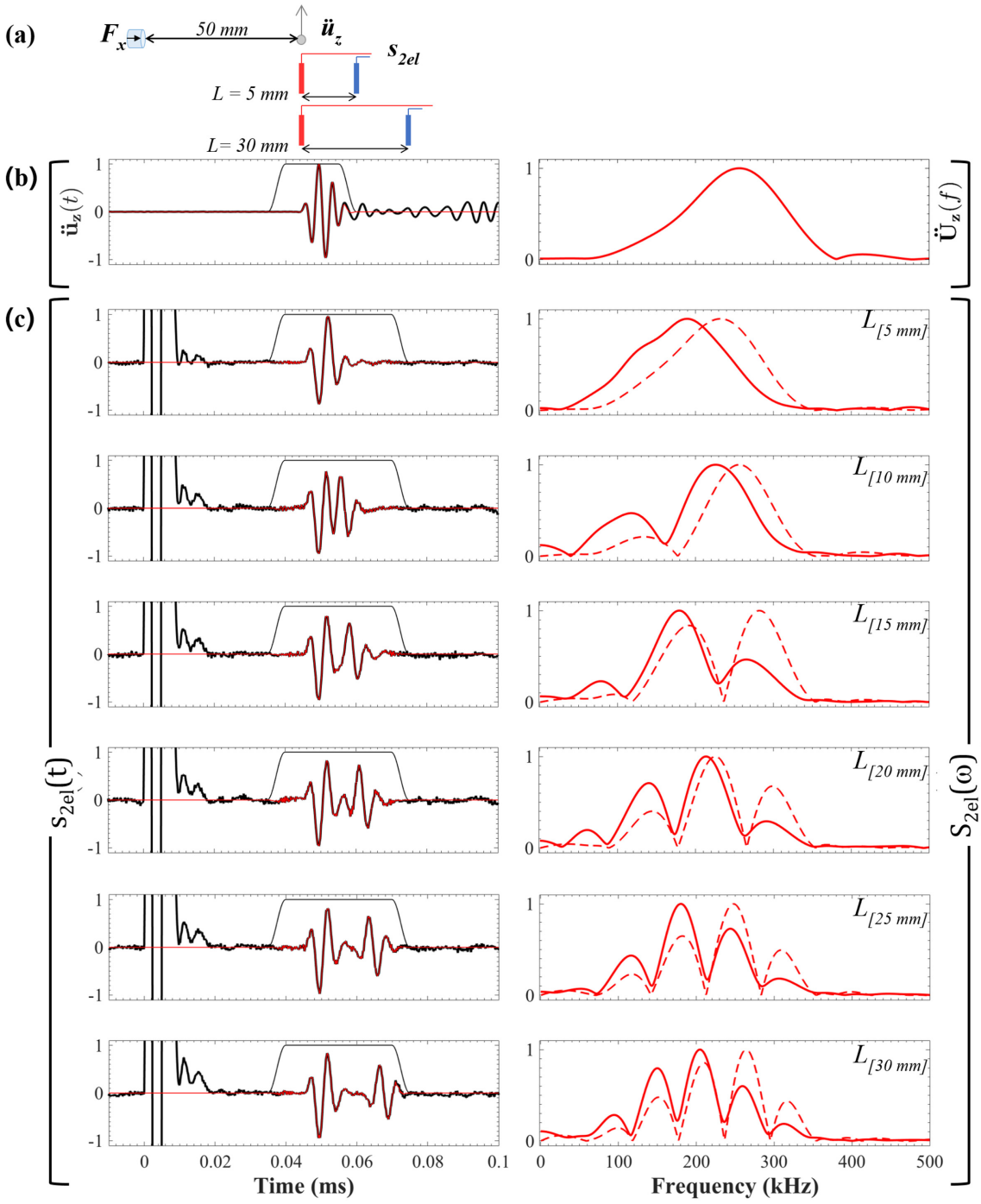

Figure 6. (a) Sketch of the acquisition for the two-electrode array. Outer electrode is displaced so that the L varies from 5 to 30 mm. (b) Seismic acceleration acquired at an offset of 50 mm (top) followed by (c) seismoelectric recordings for the different offset (left) and corresponding normalized observed (plain lines) and predicted (dashed lines) spectra (right).

4.1 Influence of array length

The spacing between the two outer electrodes L determines the time delay taken by the seismic wave to reach each electrode, which strongly impacts the resulting seismoelectric waveforms. To experimentally study this influence, seismoelectric data have been acquired using a source frequency of 200 kHz, an apparent velocity of 1850 m s^{-1} ($\alpha = 0^{o}$) and an array length L ranging from 5 mm to 30 mm for two-electrode and three-electrode arrays. The incident seismic wavelength is about 9.25 mm at 200 kHz.

Seismic and seismoelectric data have been analysed in time and frequency domains (Fig. 6). For array lengths larger than the wavelength λ, the electrical signature of the incident seismic P-wave starts decoupling into a constant arrival reaching inner electrode at around 0.046 ms and another one whose arrival time varies with the location of the outer electrode. Consequently, two-electrode acquisitions using large spacing compared to the wavelength create additional electrical signals not necessarily related with local seismoelectric fields. In the frequency domain, seismoelectric spectra

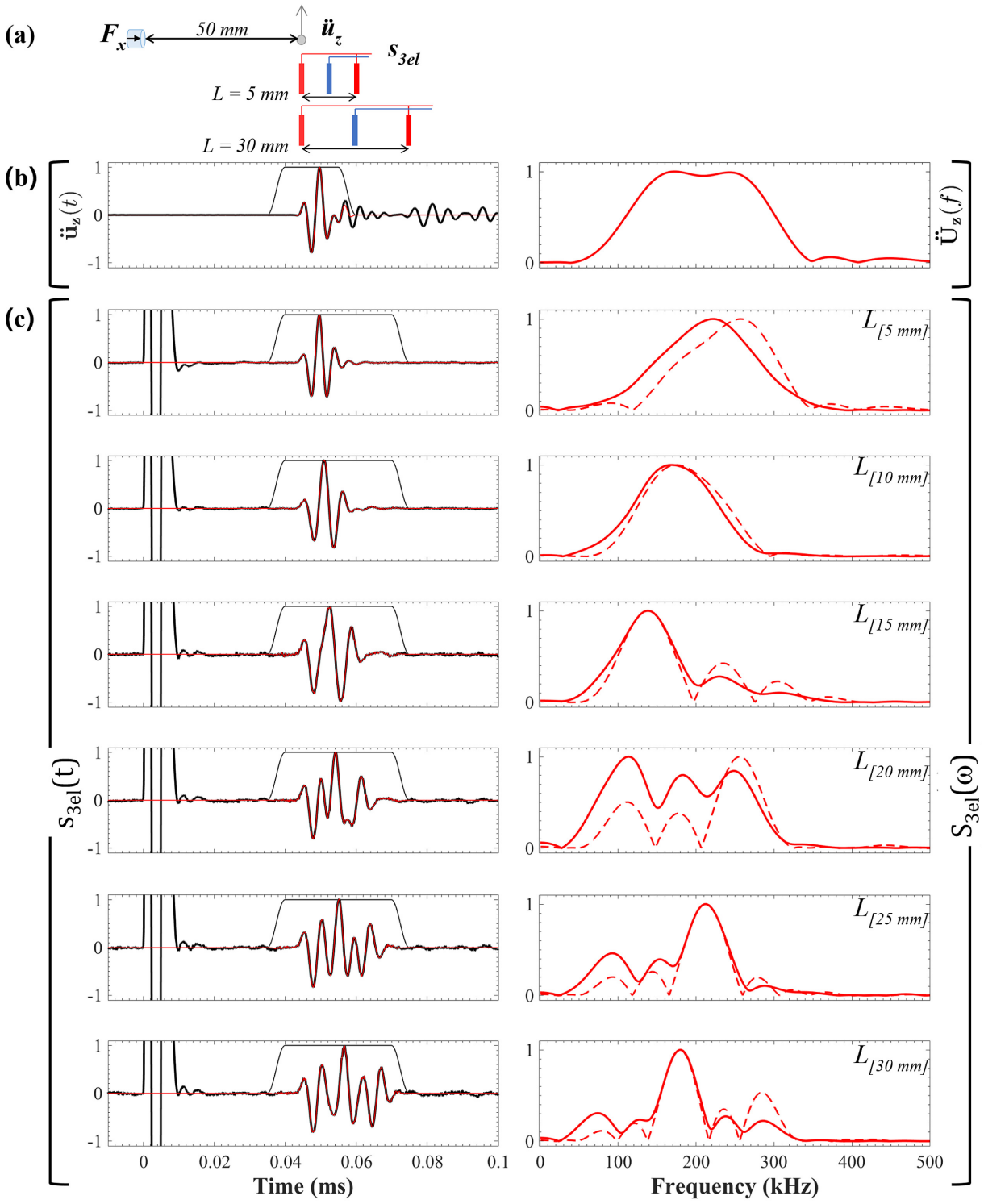

Figure 7. (a) Sketch of the acquisition for the three-electrode array. Outer and middle electrodes are displaced so that L varies from 5 to 30 mm. (b) Seismic acceleration acquired at an offset of 50 mm (top) followed by (c) seismoelectric recordings for the different offset (left) and corresponding normalized observed (plain lines) and predicted (dashed lines) spectra (right).

varies a lot depending on the outer electrode location, showing an increasing number of lobes when spacing increases. The comparison between normalized seismoelectric observations $s_{iel}(\omega)$ and the analytical frequency response of the two-electrode filter $\ddot{u}_z(\omega) \cdot G_{2el}(\omega)$ is remarkably consistent for all the spacings.

The influence of array length was also analysed in time and frequency domains for the three-electrode configuration (Fig. 7). In this experiment, we kept the same source frequency and the same position of the inner electrode for all the tested array lengths. As for the dipole arrangement, the seismoelectric signals $s_{3el}(t)$ acquired

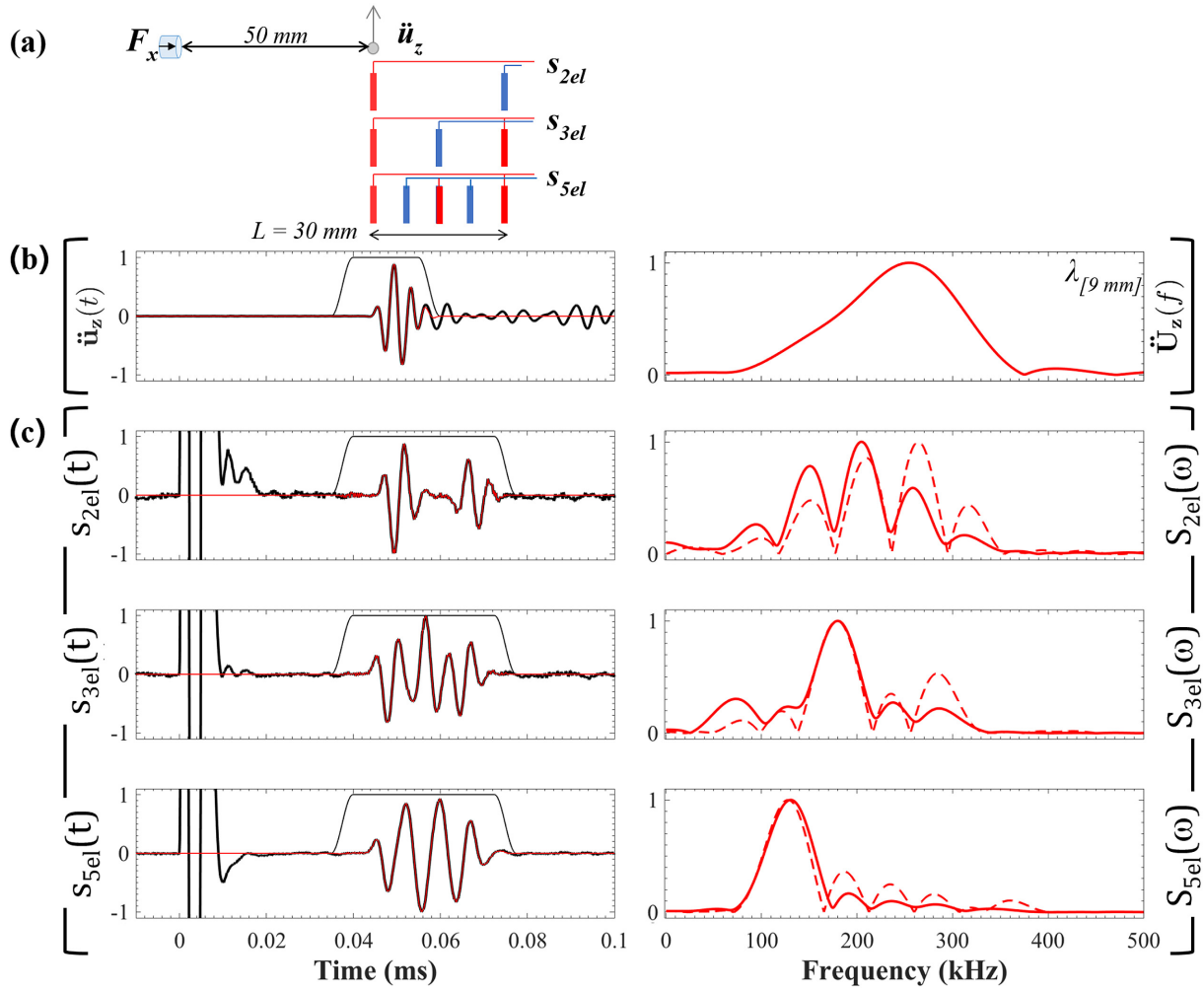

Figure 8. Influence of the number of electrodes involved in the recording array. (a) Sketch of the recording configuration. (b) Vertical acceleration recorded at 50 mm. (c) Seismoelectric measurements for the different arrays (left) and corresponding normalized observed (plain line) and predictions (dashed lines) spectra for two-electrode, three-electrode and five-electrode arrays, with an array length $L = 30$ mm.

using the three-electrode arrangement were compared with the vertical seismic acceleration spectrum $\ddot{u}_z(\omega)$ acquired nearby the inner electrode. Unlike the two-electrode results, there is no clear signal decoupling appearing in the time domain when L is increasing, but we rather observe complex time responses with interferences. For small L (lower than 15 mm), the acquisition configuration acts as a low-pass filter. Then, various lobes appear when L increases. Again, the comparison of observations and analytical predictions is successful for all array lengths.

4.2 Influence of electrode number

As suggested by the analytical filter functions, the number of electrodes involved in the recording should strongly impact the waveforms. By keeping the same source frequency of 200 kHz, the same apparent velocity of 1850 m s^{-1} ($\alpha = 0^{\circ}$) and the same electrode array length L of 30 mm, we analysed the influence of the number of the electrodes on seismoelectric signals (Fig. 8). The seismic accelerations (a) were obtained by placing a measurement point nearby the first electrode (50 mm) for each electrode configuration.

The seismoelectric waveforms no longer mimic the seismic acceleration waveforms, because the array length is much larger than the seismic wavelength. These seismolectric time waveforms $s_{iel}(t)$ are different depending on the number of electrodes involved in the acquisition. In the frequency domain, the seismoelectric signals spectra $S_{iel}(\omega)$ strongly differ according to the configuration. They are consistent with the theoretical predictions deduced from the analytical filter response with the presence of multiples lobes. Using this array length, the five-electrode arrangement acts as a low-pass filter: at 200 kHz, the seismoelectric response is maximum with the two-electrode configuration and almost cancelled with the five-electrode configuration. This figure shows that the multielectrode configuration is useful to attenuate the *P*-direct coseismic signature at a given frequency for a given apparent velocity and array length. Thus, in order to enhance or attenuate some arrivals in a seismoelectric acquisition, the electrode arrangement should be considered as a natural tool for amplification/attenuation of certain arrivals.

4.3 Influence of apparent velocity

The analytical filter response indicates that the seismoelectric signals are also affected by the apparent velocity of the seismoelectric wave when reaching the electrode arrangement. This property

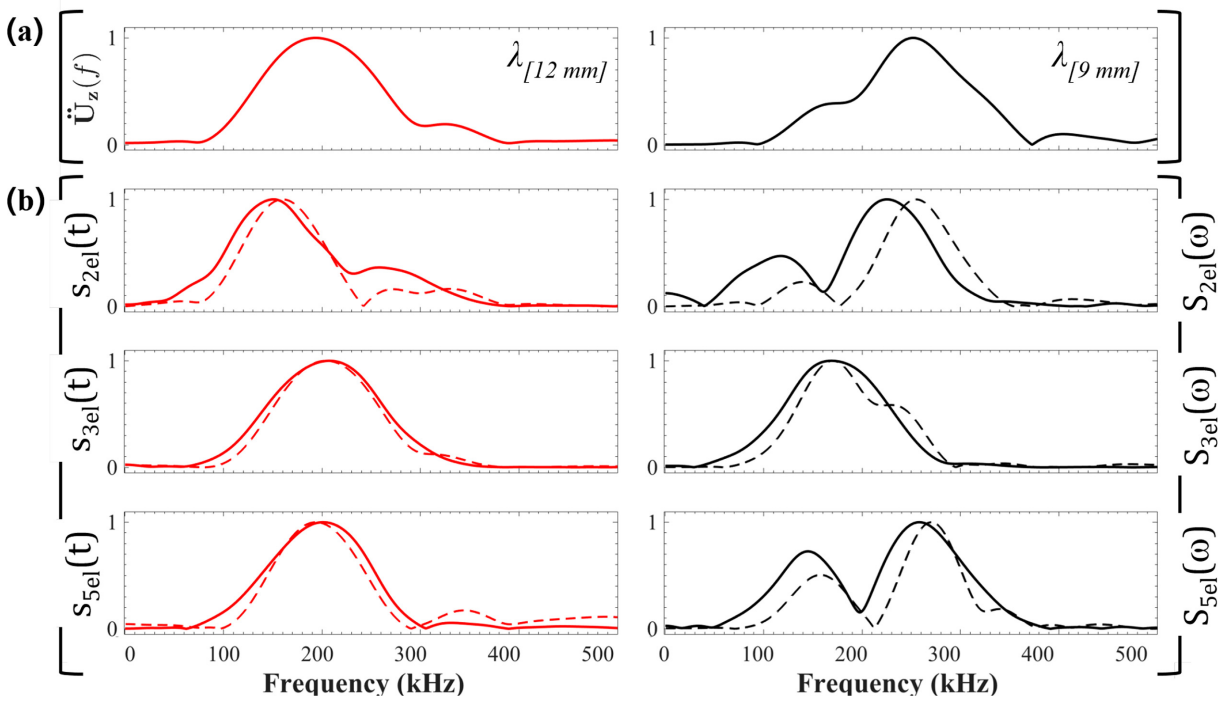

Figure 9. (a) Vertical acceleration recorded at 50 mm for two experiments performed with different apparent seismic velocities of 2460 m s^{-1} (left) and 1850 m s^{-1} (right). (b) Normalized seismoelectric observed (plain lines) and predicted (dashed lines) spectra for the different arrays and the two apparent velocities. The array length L was 10 mm.

Table 3. Computed velocities of the different waves involved in the *PSVTM* mode at 200 kHz.

Computed velocity	Material 1	Material 2
Fast *P*-wave velocity V_{Pf} (m s^{-1})	1856	3004
Slow *P*-wave velocity V_{Ps} (m s^{-1})	421	673
S-wave velocity V_S (m s^{-1})	548	1743
EM-wave velocity V_{EM} (m s^{-1})	3.43×10^6	4.85×10^6

may have a strong impact in seismoelectric exploration as the apparent velocities are hugely different according to the nature of the seismoelectric signals : coseismic waves (seismic velocity) or depth-generated EM disturbances at an interface (EM velocity).

In order to experimentally assess the sensitivity of seismoelectric signals to different apparent velocities, we adapted the source-receiver configuration, by rotating the line of receivers by a certain angle α (Fig. 1). Using an angle of $\alpha \simeq 40^o$, we have notably realized an acquisition with an apparent velocity measured around $\sim$2460 m s^{-1} for a source frequency of 200 kHz, whereas is was measured around 1850 m s^{-1} when $\alpha = 0^o$. Among all the available traces, analysis of the seismoelectric responses of the two-, three- and five-electrode configurations for this apparent velocity are presented for an offset of 77.5 mm in the time and frequency domains (Fig. 9). These results can be directly compared with identical acquisitions performed with no angle, that is, an apparent velocity of 1850 m s^{-1} (Fig. 9).

These figures show that the seismoelectric responses exhibit a large sensitivity to the apparent velocity, both in time and frequency domains and that this sensitivity differs according to the electrode arrangement. Larger changes are observed for the two-electrode and five-electrode arrays, whose frequency patterns dramatically change according to velocity, with the presence of two lobes in the low velocity case. Again, theoretical predictions of the seismoelectric responses match remarkably well the observed seismoelectric responses, for the two studied velocities and for all electrode arrangements.

This experimental sensitivity study has confirmed that the seismoelectric waveforms and their spectral contents were primarily sensitive to the electrode array properties: number of electrodes, electrode array length and apparent velocities of the incoming waves. It also showed that the changes observed in the spectral domain can be well reproduced by a filter that describes this effect assuming time delays. We propose now to numerically confirm these features but also to simulate the expected effects of the filter on seismoelectric signals generated in non-homogeneous materials, and particularly on depth-EM disturbances created at interfaces.

5 ELECTRICAL POTENTIAL NUMERICAL INVESTIGATIONS

Numerical investigations were performed at the laboratory scale using a code that allows us to generate synthetic seismograms, electrograms and magnetograms for a variety of mechanical and EM point sources in layered saturated poro-elastic media (Garambois & Dietrich 2002). Here, full waveform computations have been performed considering a mechanical source and electrical receivers in order to i) confront coseismic laboratory data with full waveform synthetic data in a homogeneous material and ii) to numerically study the novel recording approach on depth-generated seismoelectric signals in an heterogeneous material. For these purposes, we have modified the code, originally designed to compute electrical fields, by computing the absolute electric potentials, as described in Dietrich *et al.* (2018).

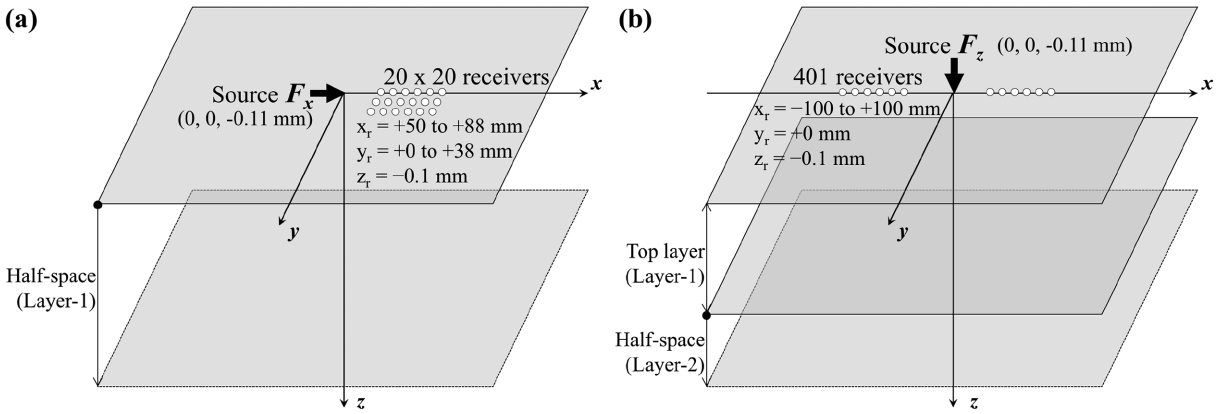

Figure 10. Sketches of the computations performed in a homogeneous layer (a) with receivers spaced on a grid and (b) in a heterogeneous layer, with receivers spread along a 2-D line.

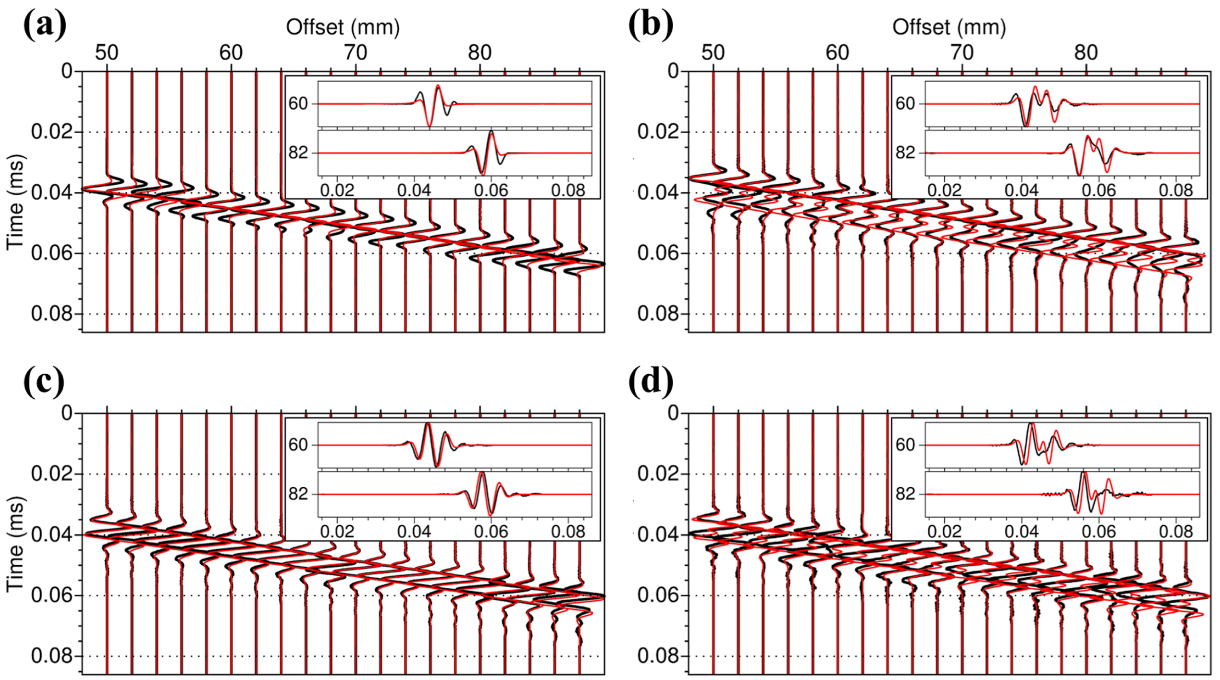

Figure 11. Comparisons between laboratory data (black) and numerical simulations (red) for the *P*-direct waves arrival propagating in material 1 with an angle $\alpha \simeq 40^o$. (a) Vertical seismic acceleration. Seismoelectric data are displayed for two-electrode (b), three-electrode (c) and five-electrode (d) arrangements. The insets zoom at two acquisition offsets : 60 and 82 mm.

5.1 Homogeneous material: comparison with laboratory data

The first simulations were performed in a homogeneous half-space using a horizontal point force source F_x. We notably computed vertical seismic displacements $u_z(t)$, the inline electric fields $E_x(t)$, the absolute electrical potentials $v(t)$ and consequently the electric potential difference $s_{iel}(t)$ for different electrode arrangements. To mimic laboratory data, we used a zero-phase Ricker wavelet with a dominant frequency of 175 kHz.

The properties of the homogeneous medium (material 1) as well as the corresponding velocities of the propagating waves are displayed in Tables 2 and 3, respectively. They were chosen to reproduce as much as possible the material properties experimentally studied.

The simulations were performed in the *PSVTM* mode, which couples the propagation of fast *P*-waves, slow *P*-waves, shear *S*-waves polarized in the vertical plane of propagation and *EM* waves with a transverse polarization of the magnetic field (*TM*) (Dietrich *et al.* 2018). The horizontal point force F_x was placed at a depth of ($z_s = 0.1$ mm) and receivers were placed on a 20 × 20 grid in the *x*–*y* plane at a depth of $z_r = 0.11$ mm (Fig. 10). This grid enables us to compute seismic and seismoelectric data with oblique receivers, in order to reproduce the experimental study performed using an angle α for the receiver line. This grid was placed 50 mm apart from the source. The numerical data were computed with a 10 MHz sampling rate on a 0.124 ms time window.

The results of the numerical simulations are displayed in Fig. 11, the seismic acceleration $\ddot{u}_z(t)$ and the seismoelectric responses $s_{iel}(t)$ for two-, three- and five-electrode configurations (red curves) are displayed. These results are directly compared in the time domain

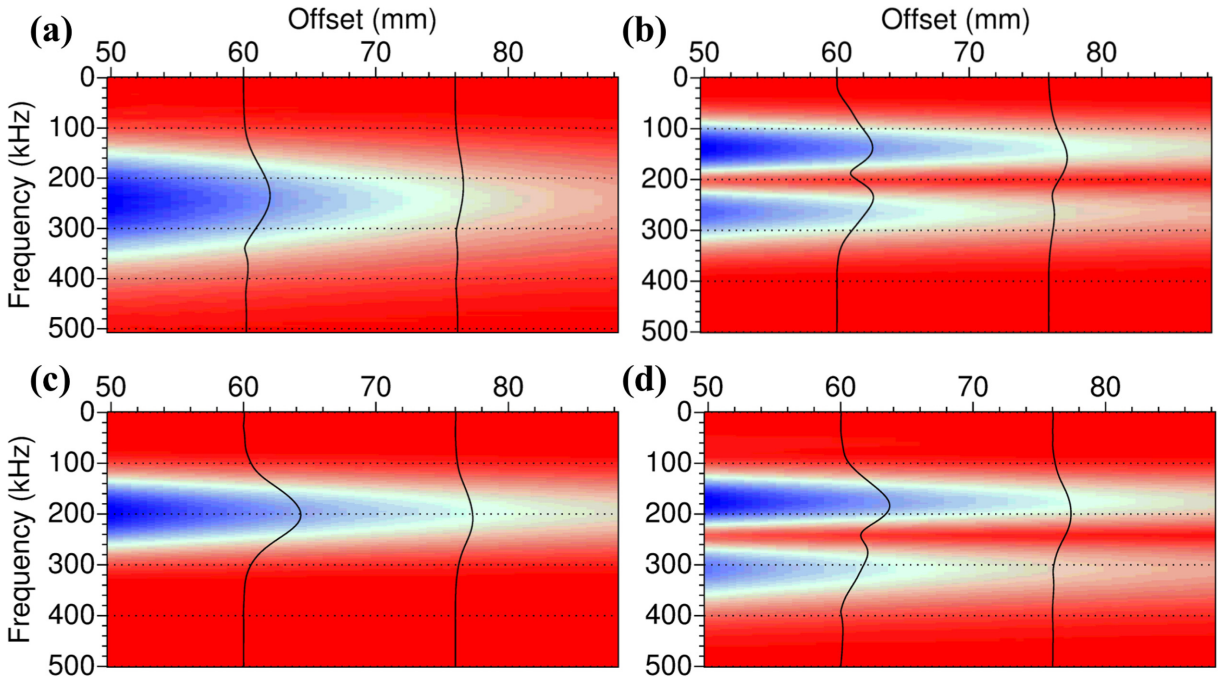

Figure 12. Spectral amplitudes versus offset of the acceleration (a) and seismoelectric synthetic data obtained using the two-electrode (b), three-electrode (c) and five-electrode (d) configurations. The black curves show the experimental spectra obtained for two traces located at 60 and 76 mm.

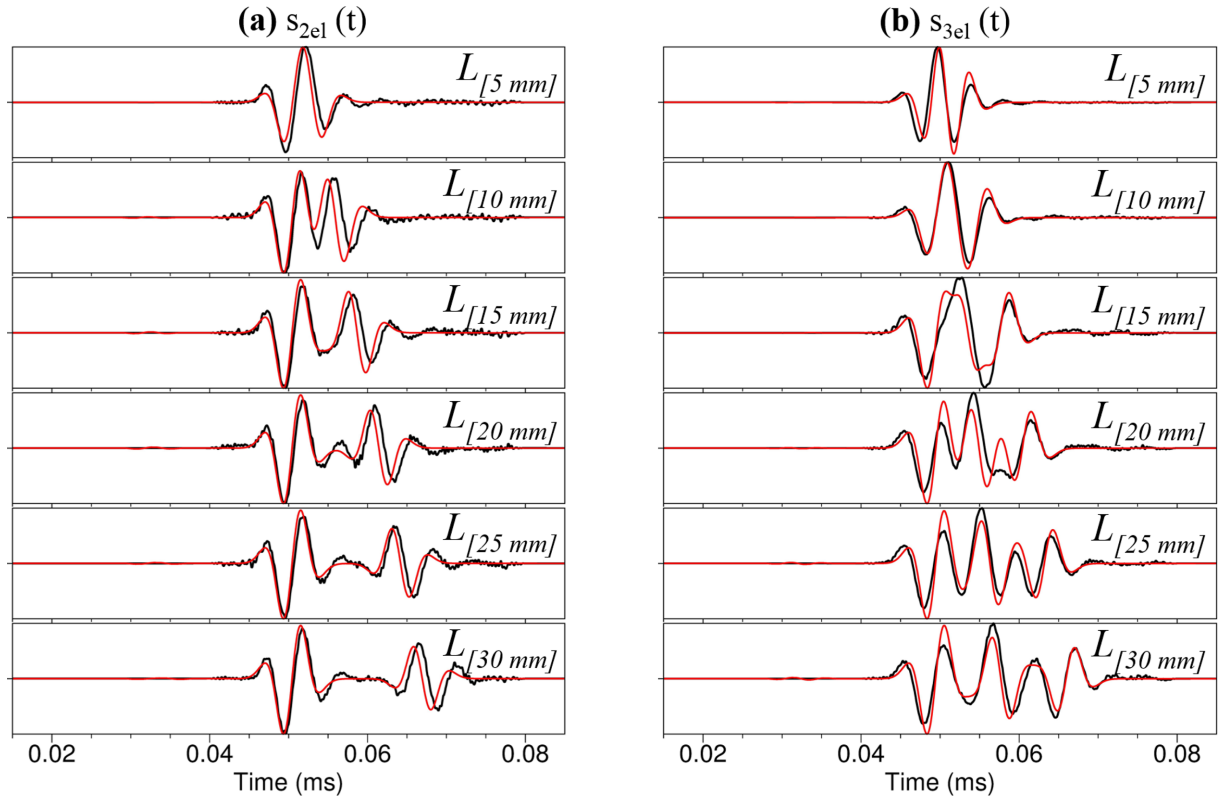

Figure 13. Numerical (red curve) and laboratory (black curve) normalized seismoelectric data acquired for an inner electrode located at 50 mm from the 200 kHz source. The two-electrode (a) and three-electrode (b) configurations are compared for various array lengths L. Numerical computations were made considering homogeneous material 1.

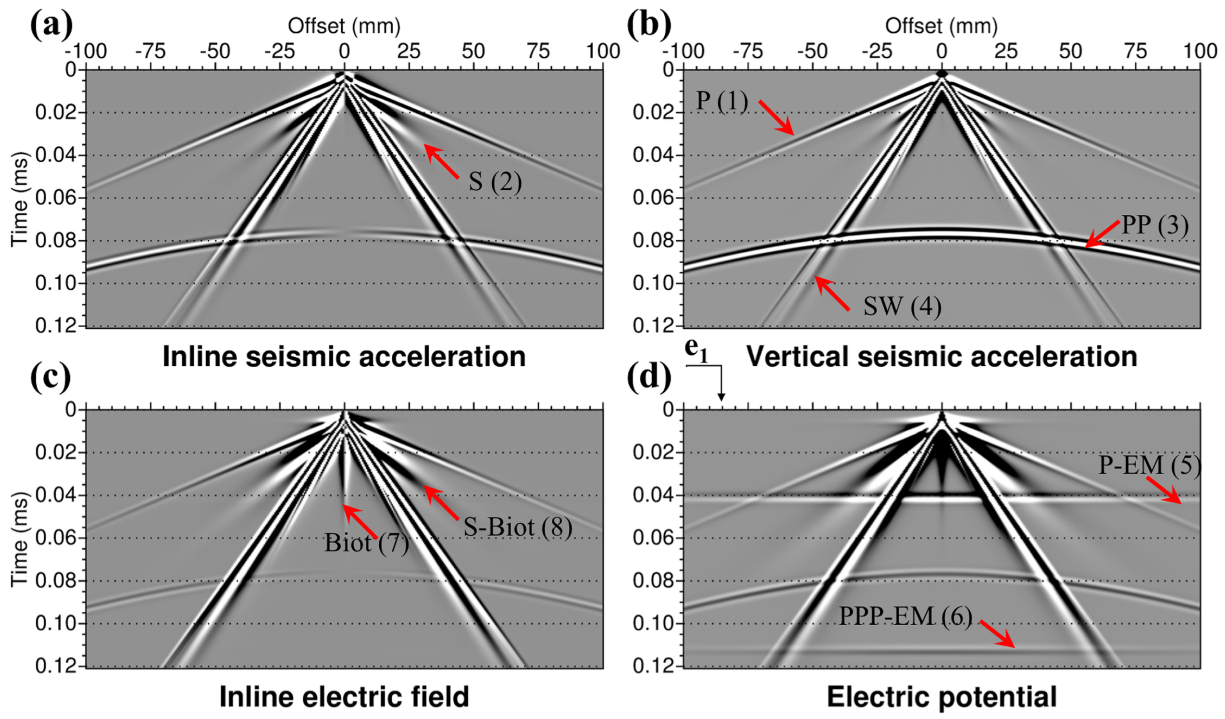

Figure 14. Numerical computations of longitudinal seismic acceleration $\ddot{u}_x(t)$ (a), vertical seismic acceleration $\ddot{u}_z(t)$ (b), seismoelectric field $E_x(t)$(c) and absolute electrical potential $v(t)$ (d) generated by a vertical point source in a two-layer model.

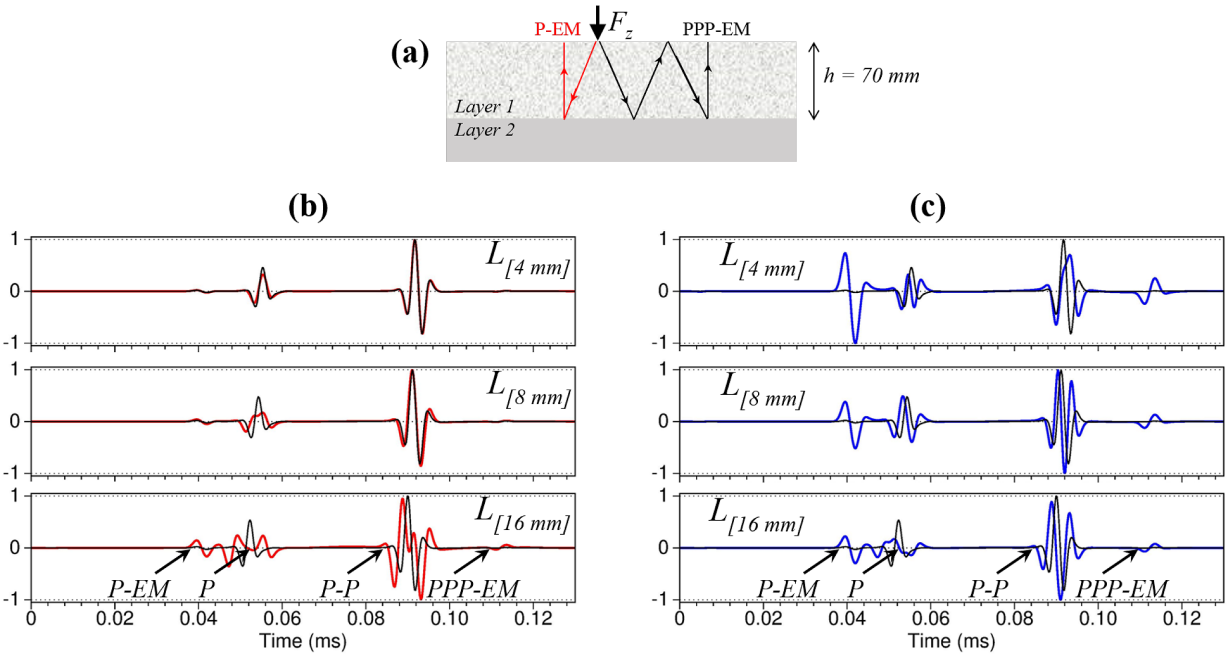

Figure 15. (a) Sketch of the two depth-generated seismoelectric disturbances. (b) Superimposition of the seismoelectric field (black) and the voltage difference (red) obtained for different array lengths. (c) Superimposition of the seismoelectric field (black) and the signal s_{3el} obtained for different array lengths. The inner electrode was located at an offset of −84 mm. The *P*-wave wavelength equals approximately 9.1 mm.

with laboratory data after tapering and normalization (blue curves). Overall, the synthetic and experimental data are remarkably consistent, for both the seismic and the seismoelectric data, whatever the electrode configuration used. The variations of spectral amplitudes of seismic and seismoelectric synthetic responses versus offset are displayed in Fig. 12. The mean frequency of seismic spectral accelerations is around 250 kHz, while seismoelectric spectral amplitudes are totally different for the two- and five- electrode configurations characterized by one main lobe and one side lobe. Their spectra diverge from the spectrum of the three-electrode configuration which only exhibits one main lobe, shifted toward 200 kHz and with a lower extend than seismic acceleration. They are consistent with laboratory data represented in black curves in Fig. 12 for two offsets (60 and 76 mm).

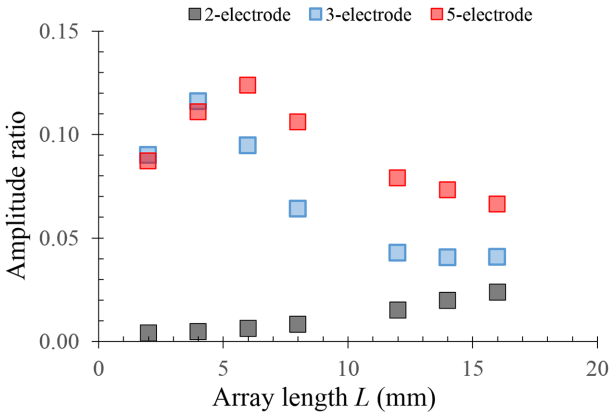

Figure 16. Amplitude ratio of interface response to coseismic electrical arrival according to array length for various array arrangements. The incoming seismic waves has a wavelength $\lambda \simeq 9.1$mm.

Additional numerical simulations have been performed to study the influence of the array length on seismoelectric waveforms, which was experimentally studied (Fig. 6) for two- and three-electrode configurations. Fig. 13 shows the superimposition of laboratory data (blue line) with numerical data (red line) for the two-electrode (a) and three-electrode (b) configurations and L ranging from 5 mm to 30 mm. Although the waveforms do not exactly match, the comparison shows consistent results notably exhibiting two arrivals that separate clearly when L is increasing for the two-electrode configuration. In addition, the main features describing the complexity of the waveforms with increasing L for the three-electrode configuration are well described by the numerical approach, although minor phase shifts can be observed.

This comparison between experimental and numerical approaches indicates that the absolute electrical potential approach developed by Dietrich *et al.* (2018) in the original numerical code of Garambois & Dietrich (2002) reproduces fairly laboratory data and particularly the filtering effect due to the electrode arrangement. For this reason, it appears interesting to extend the study to non-homogeneous materials in order to predict the influence of the electrode configuration on seismoelectric signals generated at deep interfaces, in laboratory conditions.

5.2 Implications in the presence of an interface

Full waveform computations of the seismoelectric response considering different electrode arrangements have been performed with a simple two-layer model by considering a vertical point force F_z and by including the free surface effects. The model used in this study is a 70 mm thick layer composed of material-1 overlying an half-space composed of harder material-2 (Tables 2 and 3). All traces were computed over a duration of 1 ms with 4096 samples, which corresponds to a Nyquist frequency of 2048 kHz. The source time function is a zero-phase Ricker wavelet having a dominant frequency of 200 kHz. The seismic source is located at a depth $z_s =$ 1.1 mm, while the 401 receivers are located at a depth $z_r =$0.1 mm, between $-$100 and 100 mm along the x-axis (Fig. 10).

Fig. 14 shows the seismograms (a and b), the electric field (c) and the absolute electrical potential (d) computed for the two-layer model. Several different arrivals appear on the seismograms: direct P (1) and S waves (2), reflection PP at the interface (3) and Rayleigh waves (4). On the inline electric field section $E_x(t)$, the signature of Biot-slow waves (7) are present at low offsets in the diffuse regime (low frequency event located only nearby the source) and also in the propagative regime resulting from a conversion from S to Biot slow wave at the free surface (8). These identifications were possible thanks to the flexibility of the code to compute only partial solutions of wave conversions at any interface. Despite having multiplied the seismic to EM reflection coefficient by a factor of 10 at the interface, no clear EM disturbances can be observed on the E_x section. This is the main difference with the electrical potential section, which clearly shows a large EM-disturbance arriving at 0.038 ms (5), which corresponds to the time taken by the seismic wave to reach the interface at depth 70 mm. We can even observe a multiple of this event at 0.115 ms (6) corresponding to a multiple P-wave reflection reaching the interface after 210 mm propagation. This example illustrates well how depth-generated EM waves are strongly attenuated when an electric field is recorded and how they are clearly observed when absolute electrical potentials are measured.

The relative amplitudes of the different arrivals according to electrode arrangement and to various electrode array lengths are displayed in Fig. 15. They are shown for an inner electrode e_1 located at 84 mm from the source. Considering depth-generated EM disturbances (5), there is a huge relative amplitude difference according to the electrode arrangement: it is strongly attenuated with the two-electrode arrangement while amplitude is almost maximum when three- and five-electrode are used. This relative amplitude difference decreases when L increases. Variations of the electric signals associated with the coseismic P-wave reflected events (P and PP) are relatively weak whatever the number of electrodes or the array length used.

To better quantify this crucial observation, we computed the amplitude ratio between interface response signals and coseismic P–P reflected electric signals for the different array arrangements and various array lengths by measuring their maximal values (Fig. 16). The effect of multiplying the EM interface response by a factor of 10 has been removed from the analysis so that the ratios presented here are the real one. It shows huge ratio differences depending on the type of electrode array and also on the array length. This numerical experiment clearly indicates that the use of a dipolar configuration is not suited to record depth-generated EM wave as it will favour the recording of coseismic seismoelectric signals. On the contrary, more complex three- and five-electrode configurations with low L (of the order of the coseismic signals wavelengths) should be used, in order to increase the relative amplitude of the EM disturbances. This original result should improve the detection of these depth-generated EM disturbances and consequently could revive seismoelectric exploration.

6 CONCLUSIONS

In this study, we have experimentally investigated at the laboratory scale the potential and benefits of using arrays of electrodes to record seismoelectric data. We have confirmed both experimentally and numerically that the electric signals can be described using a filter theory, as proposed by Dietrich *et al.* (2018). The seismoelectric recorded waveforms are strongly influenced by this filter which is strongly sensitive to the number of electrodes, to the spacing between these electrodes and to the apparent seismic wave velocity. This filtering effect has a strong influence in the seismoelectric spectral pattern and should consequently be taken into account when analysing quantitatively coseismic signals.

By extending these results, we can conclude that the choice of the electrode configuration, which can be analytically predicted, can be used as a spatial filter able to attenuate noise and coseismic electric signals in order to facilitate detection of depth-generated seismoelectric signals, in a given frequency range. In particular, we have demonstrated that the dipolar acquisition classically used in seismoelectric observations is particularly unfavourable to detect seismoelectric signals originating from an interface, that is, with large apparent velocities. For this purpose, more complex configurations involving three to five electrodes with adapted spacings should be used. This observation might explain the difficulty in recording interesting seismoelectric signals generated at interfaces and thus suggest news acquisition strategies to revive seismoelectric imaging, which has been proved to be particularly sensitive to fluid's or chemistry contrasts compared to seismic reflection method.

ACKNOWLEDGEMENTS

This work has been supported by a grant from Labex OSUG@2020 (Investissements d'Avenir - ANR10 LABX56) and by a PhD scholarship from the research french Ministry. The laboratory experiments were performed at Laboratoire des Fluides Complexes et leurs Réservoirs, UMR 5150 Univ Pau & Pays Adour, CNRS, TOTAL.

REFERENCES

Beamish, D., 1999. Characteristics of near-surface electrokinetic coupling, *Geophys. J. Int.,* **137,** 231–243.

Block, G.I. & Harris, J.G., 2006. Conductivity dependence of seismoelectric wave phenomena in fluid-saturated sediments, *J. geophys. Res.,* **111**(B01304), 1–12.

Bordes, C., Jouniaux, L., Garambois, S., Dietrich, M., Pozzi, J.-P. & Gaffet, S., 2008. Evidence of the theoretically predicted seismo-magnetic conversion, *Geophys. J. Int.,* **174,** 489–504.

Bordes, C., Senechal, P., Barriere, J., Brito, D., Normandin, E. & Jougnot, D., 2015. Impact of water saturation on seismoelectric transfer functions: a laboratory study of coseismic phenomenon, *Geophys. J. Int.,* **200,** 1317–1335.

Broding, R.A., Buchanan, S.D. & Hearn, D.P., 1963. Field experiments on the electroseismic effect, *IEEE Trans. Geosci. Electron.,* **GE-1**(1), 23–31.

Bulychov, A.A., 2003. Seismic-electric effect experiments on shallow subsurface geological cross-section, in *65th EAGE Conference & Exhibition,* Earthdoc, **P098,** 1–4.

Bulychov, A.A., 2005. Near surface kimberlites: new data on seismoelectric effect experiment, in *67th EAGE Conference & Exhibition,* Earthdoc, **P322,** 1–4.

Butler, K.E. & Russell, R.D., 2003. Cancellation of multiple harmonic noise series in geophysical records, *Geophysics,* **68**(3), 1083–1090.

Butler, K.E., Russell, R.D., Kepic, A.W. & Maxwell, M., 1996. Measurement of the seismoelectric response from a shallow boundary, *Geophysics,* **61**(6), 1769–1778.

Chen, M. & Mu, Y., 2005. Experimental studies of seismoelectric effects in fluid-saturated porous media, *J. Geophys. Eng.,* **2,** 222–230.

Dean, T. & Valuri, J., 2012. A brute-strength approach to improving the quality of seismoelectric data, in *SEG Technical Program Expanded Abstracts,* pp. 1–6.

Dietrich, M., Devi, M.S., Garambois, S., Brito, D. & Bordes, C., 2018. A novel approach for seismo-electric measurements using multielectrode arrangements: I - theory and numerical experiments, *Geophys. J. Int.,* submitted.

Dupuis, J.C., Butler, K.E. & Kepic, A.W., 2007. Seismoelectric imaging of the vadose zone of a sand aquifer, *Geophysics,* **72**(6), A81–A85.

Dupuis, J.C., Butler, K.E., Kepic, A.W. & Harris, B.D., 2009. Anatomy of a seismoelectric conversion: measurements and conceptual modeling in boreholes penetrating a sandy aquifer, *J. geophys. Res.,* **114**(B10), B10306, pp. 1–9.

Garambois, S. & Dietrich, M., 2001. Seismoelectric wave conversions in porous media: Field measurements and transfer function analysis, *Geophysics,* **66**(5), 1417–1430.

Garambois, S. & Dietrich, M., 2002. Full waveform numerical simulations of seismo-electromagnetic wave conversions in fluid-saturated porous media, *J. geophys. Res.,* **107**(B7), ESE 5-1–ESE 5-18.

Glover, P. W.J. & Dery, N., 2010. Streaming potential coupling coefficient of quartz glass bead packs: Dependence on grain diameter, pore size, and pore throat radius, *Geophysics,* **75**(6), F225–F241.

Haines, S.S., Guitton, A. & Biondi, B.L., 2007a. Seismoelectric data processing for surface surveys of shallow targets, *Geophysics,* **72**(2), G1–G8.

Haines, S.S., Guitton, A. & Biondi, B.L., 2007b. Seismoelectric imaging of shallow targets, *Geophysics,* **72**(2), G9–G20.

Hales, F.W. & Edwards, T.E., 1955. Some theoretical considerations on the use of multiple geophones arranged linearly along the line of traverse, *Geophys. Prospect.,* **3,** 65–73.

Holzhauer, J., Brito, D., Bordes, C., Brun, Y. & Guatarbes, B., 2017. Experimental quantification of the seismoelectric transfer function and its dependence on conductivity and saturation in loose sand, *Geophys. Prospect.,* **65,** 1097–1120.

Ivanov, A.G., 1939. Effects of electrization of earth layers by elastic waves passing through them (in Russian), *Dokl. Akad. Nauk SSSR,* **24**(1), 42–45.

Jouniaux, L. & Zyserman, F., 2016. A review on electrokinetically induced seismo-electrics, electro-seismics, and seismo-magnetics for earth sciences, *Solid Earth,* **7,** 249–284.

Kepic, A.W. & Butler, K.E., 2002. The art of measuring very low amplitude seismoelectric signals, in *64th EAGE Conference & Exhibition,* p. 193.

Knapp, R.W. & Steeples, D.W., 1986a. High resolution common-depth-point reflection profiling: instrumentation, *Geophysics,* **51**(2), 276–282.

Knapp, R.W. & Steeples, D.W., 1986b. High resolution common-depth-point reflection profiling: field acquisition parameter design, *Geophysics,* **51**(2), 283–294.

Lebedev, M., Bona, A., Pevzner, R. & Gurevitch, B., 2011. Elastic anisotropy estimation from laboratory measurements of velocity and polarization of quasi-p-waves using laser interferometry, *Geophysics,* **76**(3), WA83–WA89.

Long, L.T. & Rivers, W.K., 1975. Field measurement of the electroseismic response, *Geophysics,* **40**(2), 233–245.

Macnae, J.C., Lamontagne, Y. & West, G.F., 1984. Noise processing techniques for time-domain EM systems, *Geophysics,* **49**(7), 934–948.

Martner, S.T. & Sparks, N.R., 1959. The electroseismic effect, *Geophysics,* **24**(2), 297–308.

Mikhailov, O.V., Haartsen, M.W. & Toksoz, M.N., 1997. Electroseismic investigation of the shallow subsurface: field measurements and numerical modeling, *Geophysics,* **62**(1), 97–105.

Norvill, M. & Kepic, A., 2004. Enhancing electrical signals with sensor arrays, in *ASEG Extended Abstract,* pp. 1–4.

Pride, S., 1994. Governing equations for the coupled electromagnetics and acoustics of porous media, *Phys. Rev. B,* **50**(21), 15 678–15 696.

Rosid, M. & Kepic, A., 2004, Using the seismoelectric method for hydrogeological investigations. *Proceedings of the EEGS annual meeting,* Denver, Colorado, USA, p. 1480–1489.

Russell, R.D., Butler, K.E., Kepic, A.W. & Maxwell, M., 1997. Seismoelectric exploration, *Leading Edge,* **16,** 1611–1615.

Schakel, M.D., Smeulders, D.M., Slob, E.C. & Heller, H.K.J., 2011. Seismoelectric interface response : experimental results and forward model, *Geophysics,* **76**(4), N29–N36.

Sorokina, T.V. & Bulychov, A.A., 2001, Seismic-electric benchmarking of shallow subsurface horizons and dome cavities. *EAGE, 63rd*

Conference & Technical Exhibition, Amsterdam, The Netherlands, p. 1–4.

Strahser, M. H.P., Rabbel, W. & Schildknecht, F., 2007. Polarisation and slowness of seismoelectric signals: a case study, *Near Surf. Geophys.,* **5,** 97–114.

Thompson, A.H. & Gist, G.A., 1993. Geophysical applications of electrokinetic conversion, *Leading Edge,* **12,** 1169–1173.

Thompson, R.R., 1936. The seismic electric effect, *Geophysics,* **1,** 327–335.

Warden, S., Garambois, S., Sailhac, P., Jouniaux, L. & Bano, M., 2012. Curvelet-based seismoelectric data processing, *Geophys. J. Int.,* **190,** 1553–1550.

Zhu, Z. & Toksoz, M.N., 2005. Seismoelectric and seismomagnetic measurements in fractured borehole models, *Geophysics,* **70**(4), F45–F51.

Zhu, Z., Toksoz, M.N. & Burns, D.R., 2008. Electroseismic and seismoelectric measurements of rock samples in a water tank, *Geophysics,* **73**(5), E153–E164.